Dynamics and Quantum Yields of $H_2 + CH_2CO$ as a Primary Photolysis Channel in CH_3CHO

Aaron W. Harrison,[a] Alireza Kharazmi,[a] Miranda F. Shaw,[b] Mitchell S. Quinn,[a] K. L. Kelvin Lee,[a,c] Klaas Nauta,[a] Keiran N. Rowell,[a] Meredith J. T. Jordan*[b] and Scott H. Kable*[a]

[a] School of Chemistry, University of New South Wales, Sydney, NSW 2052.

[b] School of Chemistry, University of Sydney, Sydney, NSW, 2006

[c] Present address: Harvard-Smithsonian Institute for Astrophysics

* Corresponding authors: s.kable@unsw.edu.au; meredith.jordan@sydney.edu.au

SUPPLEMENTARY INFORMATION

Index

I. Methods
a) Experimental

For the present work, acetaldehyde (>99%, Sigma-Aldrich) samples were degassed and purified using the freeze-pump-thaw technique. The vapor was then mixed with He gas in a cylinder at a concentration of 5% sample in He. This mixture was then expanded into the vacuum chamber at a backing pressure of 200-250 kPa at 20 Hz repetition rate using a Parker Series 9 solenoid valve. After passing through a 1 mm skimmer, the jet-cooled sample was photolysed with the frequency-doubled output from a dye laser (305-323 nm, 1.5-3 mJ/pulse), which was pumped by the 2nd harmonic of a Nd:YAG laser. The earliest part of the molecular beam was interrogated to minimize/avoid cluster formation. The molecular hydrogen (H_2) product was then ionised (pump-probe delay of 50 ns) with one of two dye laser configurations depending on the ionisation wavelength used. For wavelengths from 200-208 nm, a 532 nm-pumped dye laser equipped with a third harmonic generation (THG) setup was used for ionisation. Wavelengths from 208-218 nm were obtained by using the frequency-doubled output of a dye laser pumped by the 3rd harmonic of an Nd:YAG laser (355 nm). Typical ionisation laser power was ~1-2 mJ/pulse and was focused into the chamber using a 500 mm lens. To correct for power fluctuations while collecting he ionisation spectra, the laser power was monitored with a photodiode.

Following ionisation, the H_2^+ ions are formed in the ion optics regions of the vacuum chamber. The velocity-map imaging (VMI) electrodes[1] consist of repeller and extractor electrodes with voltages set to +2700 V and +2000 V, respectively, with all other electrodes maintained at ground. The recoiling ion sphere was propagated through the time-of-flight (TOF) region of a mass spectrometer and detected by a Chevron-stack of microchannel plates (75 mm diameter) coupled to a P20 phosphor screen. Ion arrival times and intensities for ionisation spectra were obtained using a photomultiplier tube adjacent to the phosphor screen.

For the H_2 ionisation spectroscopy and imaging, the detector was gated to detect ions with *m/z* of 2 by applying a negative voltage pulse to the front MCP (-450 V). As the Doppler width of the H_2 fragments (~5 cm^{-1}) exceeded that of the ionization laser bandwidth, the H_2 images were collected by scanning the laser over the Doppler profile. There was a very minor probe-only signal which was subtracted from was pump-probe images to remove the one-laser

background. Determination of the fragment translational energy from the VMI setup was calibrated using O^+ from O_2 photodissociation at 224.99 nm via two photon excitation of the $3d\pi(^3\Sigma_{1g})$ Rydberg state.[2]

b) Theoretical

Following Collins and coworkers,[3-5] the potential energy surface (PES), V, is expressed as a modified Shepard interpolation about N_{data} PES data points as:

$$V(\mathbf{Z}) = \sum_{g \in G} \sum_{i=1}^{N_{data}} w_{g \circ i}(\mathbf{Z}) T_{g \circ i}(\boldsymbol{\zeta}), \tag{S1}$$

for $\boldsymbol{\zeta}$ local internal coordinates defined, at each configuration, in terms of inverse atom-atom distances, $\mathbf{Z}$, and w_i normalised weight functions given by

$$w_i(\mathbf{Z}) = \frac{v_i(\mathbf{Z})}{\sum_{g \in G} \sum_{k=1}^{N_{data}} v_{g \circ k}(\mathbf{Z})} \tag{S2}$$

with the primitive weight function, v_i, given by

$$v_i(\mathbf{Z}) = \sum_{k=1}^{N(N-1)/2} \|Z - Z_k\|^{-2p}. \tag{S3}$$

for $N = 7$ atoms in the system.

In Eq. (S1), g are elements of the complete nuclear permutation and inversion (CNPI) group, G. Here we have approximated $|G| = 1$ as there is no mechanism for interchange of equivalent nuclei along the intrinsic reaction coordinate for the $CH_3CHO \rightarrow CH_2CO + H_2$ reaction. The $T_i(\boldsymbol{\zeta})$ in Eq. (S1) are second order Taylor expansion about the ith PES data point. The weight power, p, determines the relative contribution of each PES data point.

The *ab initio* second derivatives at each data point configuration, were also used to construct a zero-point energy (ZPE) surface, $ZPE(\boldsymbol{\zeta})$:

$$ZPE(\mathbf{Z}) = \sum_{g \epsilon G} \sum_{i=1}^{N_{data}} w_{g \circ i}(\mathbf{Z}) ZPE_{g \circ i}(\boldsymbol{\zeta}). \qquad (S4)$$

where the ZPE at each PES data point is half the sum of the non-imaginary harmonic vibrational frequencies. As each PES data point lies along the intrinsic reaction path, or characterizes separated equilibrium product configurations, there is no ambiguity in defining the ZPE. Following Lee *et al.*,[6] the ZPE was interpolated using a "standard" Shepard interpolation, that is, a distance-weighted interpolation with, arbitrarily, the same form of the weight function and the same value of p as the potential itself.

Classical trajectory simulations were performed on an effective PES, V_{eff}, defined as:

$$V_{\mathrm{eff}}(\mathbf{Z}) = \sum_{g \epsilon G} \sum_{i=1}^{N_{data}} w_{g \circ i}(\mathbf{Z}) \left\{ T_{g \circ i}(\boldsymbol{\zeta}) + ZPE_{g \circ i}(\boldsymbol{\zeta}) \right\}. \qquad (S5)$$

This ensured all products were formed with internal energies at least their total harmonic ZPE. It also ensured an accurate value of the exit channel barrier for formation of $CH_2CO + H_2$.
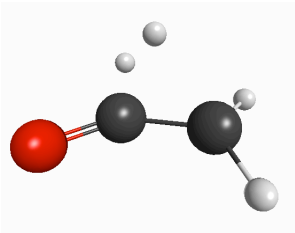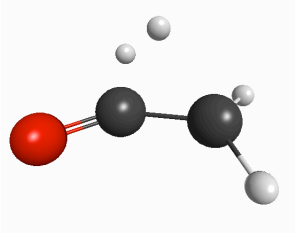
Trajectory initial conditions, constrained to model the $CH_3CHO \rightarrow CH_2CO + H_2$ transitions state, were chosen from a microcanonical distribution simulating 306 nm photolysis of acetaldehyde. Constraints were chosen to best describe the reaction coordinate at the transition state, principally the H6-H7 distance and the separation between the forming H_2 and CH_2CO molecules. Additional trajectory simulations were performed with only the four bond lengths in the four-membered ring transition state constrained. A Markov chain was used, with 500 Markov steps between initial conditions. A summary of all parameters used in the interpolation of V_{eff} and in the quasiclassical trajectory simulations is provided in Table S1. Transition state constraints are defined with respect to the atom numbering given in Figure 2 of the main text.

To validate the MP2/6-311+G(2df,p) IRC for the $CH_3CHO \rightarrow CH_2CO + H_2$ reaction, the TS was recalculated at the CCSD/6-311+G(2df,p) level of theory. The two saddle point geometries are compared in Table S2.

Table S1. Parameters used in theoretical simulations.

Parameter	Value
Potential Energy Surface Parameters:	
Electronic Structure Theory method/basis set	RMP2/6-311+G(2df,p)
Number of points in reaction path PES	76
Order of CNPI group used	1
Bond lengths defining asymptotic region of the potential	17-19 Bohr
Interpolation Parameter:	
Weight function power, p	9
Trajectory Initial Conditions:	
Initial reference geometry	RMP2/6-311+G(2df,p) saddle point for the $CH_3CHO \rightarrow CH_2CO + H_2$ reaction
Initial energy with respect to reference geometry	58.9 kJ/mol
Initial angular momentum	0
Number of Markov Steps between selection of initial conditions	500
Maximum atomic displacement per Markov Step	0.05 Bohr
Constraints used to define initial conditions (See Fig. 2 of the main text)	R(C1-H6) = 2.648 Bohr; R(C1-H7) = 2.483 Bohr; R(C2-H6) = 3.073 Bohr; R(C2-H7) = 3.960 Bohr; R(H6-H7) = 1.930 Bohr
Tolerance in constrained bond lengths	0.05 Bohr
Trajectory Simulation Parameters:	
Trajectory time-step	4.13×10^{-6} ps
Total number of trajectories	113,000
Maximum number of trajectory steps	100,000 (maximum simulation time 0.413 ps)
Number of steps between trajectory end tests	500 (corresponding to 2.06×10^{-3} ps)
Trajectory energy conservation criterion	Relative energy conservation to better than 2.5×10^{-8} (corresponding to better than 0.01 kJ/mol)
Trajectory end test criterion	Any bond length greater than 10.5 Bohr

Table S2. Optimised MP2/6-311+G(2df,p) and CCSD/6-311+G(2df,p) saddle point geometries for the $CH_3CHO \rightarrow CH_2CO + H_2$ reaction.

Method		Cartesian Coordinates (Å)		
MP2/6-311+G(2df,p):		x	y	z
	C	-0.13766	0.19573	-0.09348
	C	1.17849	-0.22415	0.01725
	O	-1.26368	-0.20746	0.01523
	H	1.94630	0.46468	-0.31092
	H	1.42878	-1.27096	0.15986
	H	0.50165	1.15430	0.65679
	H	-0.01233	1.48218	-0.17017

Imaginary frequency: 1567 cm^{-1}; Rotational constants: 64.9, 10.2 and 9.08 GHz

Method				
CCSD/6-311+G(2df,p):		x	y	z
	C	-0.14191	0.19262	-0.10080
	C	1.18153	-0.22538	0.02462
	O	-1.27038	-0.20315	0.01606
	H	1.93196	0.45243	-0.36432
	H	1.43045	-1.27239	0.16847
	H	0.56336	1.14293	0.64912
	H	-0.00046	1.49872	-0.12466

Imaginary frequency: 1636 cm^{-1}; Rotational constants: 65.0, 10.3 and 9.14 GHz

The root mean squared deviation between the MP2 and CCSD saddle point geometries is only 0.022 Å with the similarity of the geometries also seen in their respective rotational constants, as shown in Table S2. The imaginary frequencies at the saddle points are 1567 i and 1636 i cm^{-1}, at MP2/6-311+G(2df,p) and CCSD/6-311+G(2df,p), respectively, which compares to 1502 i cm^{-1}, calculated at the CCSD(T)/aug-cc-pvdz level of theory.[7] At this level of theory, reported saddle point rotational constants are 62.6, 10.0 and 8.86 GHz,[7] indicating very slight differences with respect to the MP2 and CCSD optimised geometries. The dot product of the normalized MP2 and CCSD normal coordinates corresponding to the imaginary frequencies at the saddle point is 0.9922; they are essentially identical. The similarities between MP2, CCSD and CCSD(T) saddle point geometries and imaginary frequencies and the MP2 and CCSD imaginary frequency normal coordinates indicate the MP2/6-311+G(2df,p) calculation is likely to provide an accurate representation of both the saddle point for the $CH_3CHO \rightarrow CH_2CO + H_2$ reaction and the IRC in the region of the saddle point.

II.   Photofragment Excitation Spectrum

The photofragment excitation (PHOFEX) spectrum of acetaldehyde was measured for photolysis energies ranging from 31 000 to 32 850 cm^{-1} for the $v = 0$, $J = 5$ product state of H$_2$ by scanning the photolysis wavelength and keeping the probe wavelength fixed to $Q(5)$ of the $E(0)$ - $X(0)$ transition. The resulting PHOFEX spectrum is shown in Figure S1. The feature marked with a red asterisk in this figure is the chosen photolysis energy for the H$_2$ REMPI spectra (Figure 3) and speed distributions (Figure 5).

The H$_2$ PHOFEX in the present work shows similar features as previously measured PHOFEX spectra on the CH$_3$ and HCO products[8] as well as laser-induced fluorescence measurements.[9] While the structure in this spectrum is unassigned, it has been attributed to combination bands of the CO stretch and the methyl-rocking and torsion modes of acetaldehyde[10,9] as these are the Franck-Condon active modes in the S_1-S_0 excitation. It is clear that the H$_2$ fragment yield decreases substantially with photolysis energy. This trend is largely attributed to a decrease in acetaldehyde absorption cross-section that peaks at 290 nm (34 482 cm^{-1}) and decreases as the S_1-S_0 origin is approached at ~336 nm (29 762 cm^{-1}).
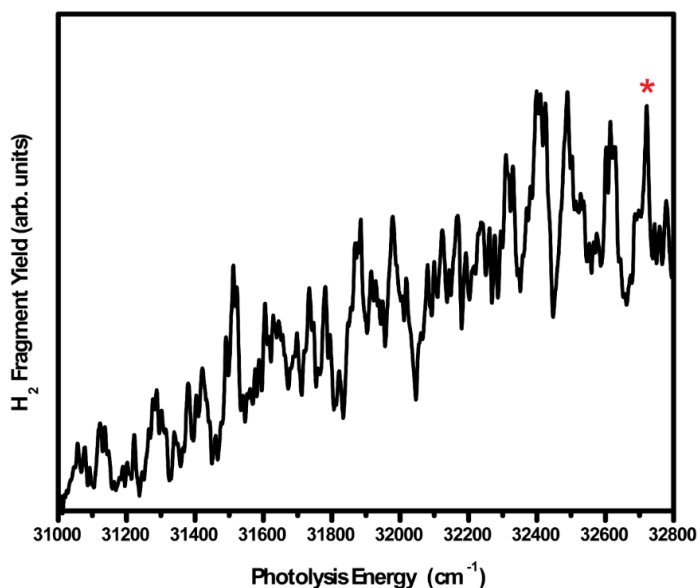

Figure S1. The photofragment excitation spectrum of CH$_3$CHO monitoring H$_2$ ($v = 0$, $J = 5$). The red star indicates the wavelength at which CH$_3$CHO was photolysed to collect H$_2$ VMI images and REMPI spectra.

III. Quasiclassical Trajectory Analysis

The trajectory simulations yielded 29 317 trajectories forming $CH_3CHO \rightarrow CH_2CO + H_2$. The results shown in the main text were obtained by constraining the five bond lengths given in Table S1 to their values at the saddle point. Standard histogram binning assigned trajectories to quantum number v if the classical H_2 vibrational energy, $E(H_2)$, is in the range $(v - \frac{1}{2}) h\nu \leq E(H_2) < (v + \frac{1}{2}) h\nu$, for ν the vibrational fundamental which has been approximated as 4000 cm^{-1} (noting that the H_2 MP2/6-311+G(2df,p) harmonic zero point energy is 2263 cm^{-1}). This yielded 26 330 trajectories with H_2 ($v = 0$), 2984 trajectories with H_2 ($v = 1$) and 1 trajectory with H_2 ($v = 2$). Because the H_2 fundamental is so large, some of the trajectories binned to a given quantum number will have vibrational energies significantly different to the corresponding quantum energy and this may affect angular momentum and translational energy distributions inferred from the simulations. The QCT H_2 vibrational energy distribution, $E(H_2)$, binned into 500 cm^{-1} bins, is shown in Figure S2.
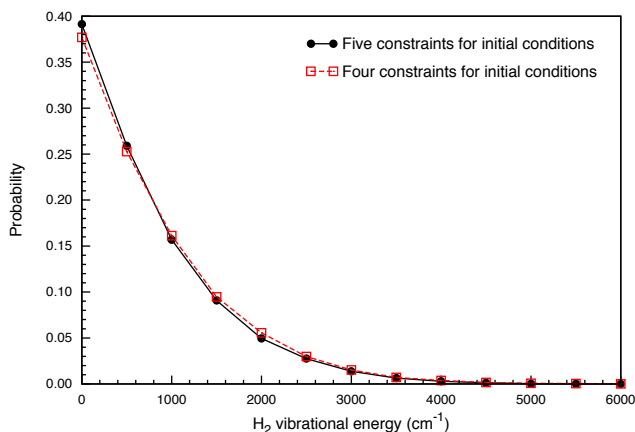

Figure S2. Classical trajectory H_2 vibrational energy distributions obtained using five (black solid line, filled black circles) and four (red dashed line, open red squares) constraints to determine trajectory initial conditions.

Figure S2 shows the $E(H_2)$ is strongly peaked at $E(H_2) \leq 500$ cm^{-1}, with probability decreasing monotonically with increasing vibrational energy. In the spirit of Gaussian binning,[11-14] we have considered narrow binning where H_2 ($v = 0$) has been assigned as $E(H_2) \leq 500$ cm^{-1}, H_2 ($v = 1$) has been assigned as $3500 < E(H_2) \leq 4500$ cm^{-1}, and so forth. This yielded

11 471 trajectories for H_2 ($v = 0$) and 271 trajectories for H_2 ($v = 1$). A comparison of QCT results using standard and narrow histogram binning is given in Figure S3.
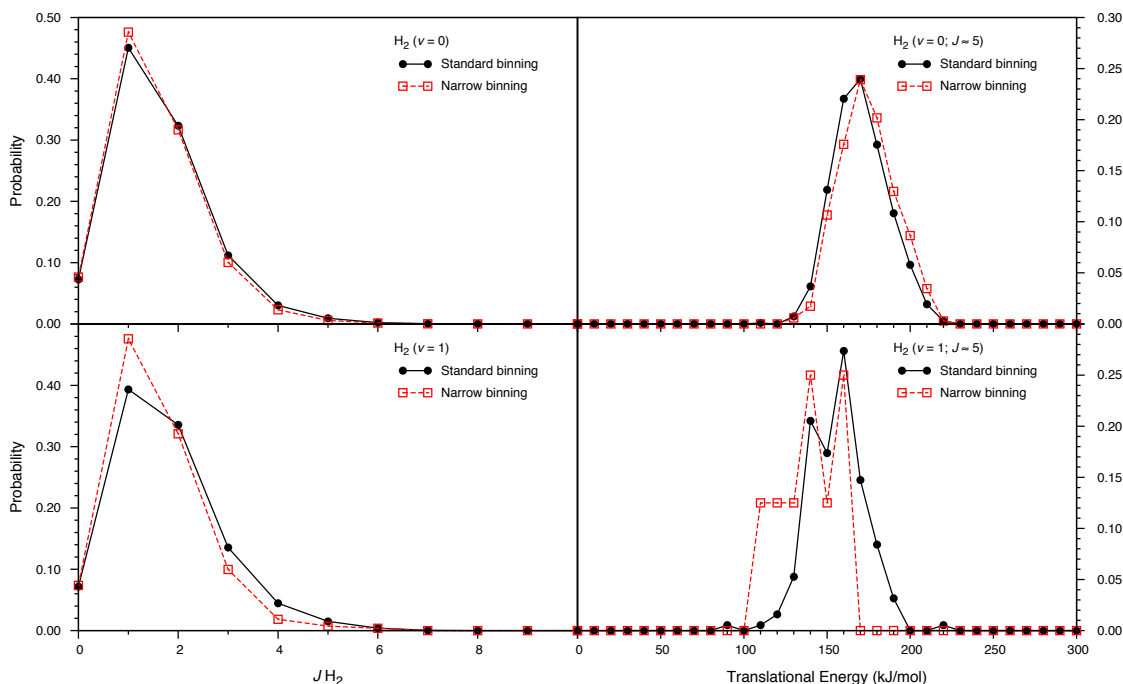

Figure S3. Quasiclassical trajectory H_2 angular momentum (left) and total translational energy (right) distributions obtained using standard (solid black lines, solid black circles) and narrow (red dashed lines, open red squares) histogram binning of H_2 vibrational states (see text).

Figure S3 shows the H_2 angular momentum distribution for H_2 ($v = 0$, $v = 1$) and the total translational energy for H_2 ($v = 0$, $v = 1$; $J \sim 5$) where $J = 5$ has been approximated as $J = 4$-6. Using standard histogram binning 1089 trajectories were obtained for H_2 ($v = 0$; $J \sim 5$) and 190 trajectories were obtained for H_2 ($v = 1$; $J \sim 5$). For narrow binning, 347 and 8 trajectories, respectively, met the H_2 ($v = 0$, $v = 1$; $J \sim 5$) criteria. As can be seen in Figure S3, neither the H_2 ($v = 0$, $v = 1$) angular momentum distributions nor the H_2 ($v = 0$; $J \sim 5$) total translational energy distribution are sensitive to the binning of the H_2 vibrational state. There may be some sensitivity to the nature of the binning for the H_2 ($v = 1$; $J \sim 5$) total translational energy distribution, where narrower binning shifts the translational energy to lower values. Because the H_2 vibrational population is a monotonically decreasing function of energy, for standard histogram binning, the average H_2 internal energy is lower, leading to larger available energy for

translation. There are, however, only small numbers of trajectories meeting the criteria for H_2 ($v = 1$; $J \sim 5$), particularly for narrow binning of the H_2 ($v = 1$) vibrational state.

The $CH_2CO + H_2$ total translational energy distributions are relatively insensitive to H_2 angular momentum state. Figure S4 compares, for H_2 ($v = 0$, $v = 1$), the total translational energy distribution for H_2 $J \sim 5$ with that summed over all H_2 angular momentum states.
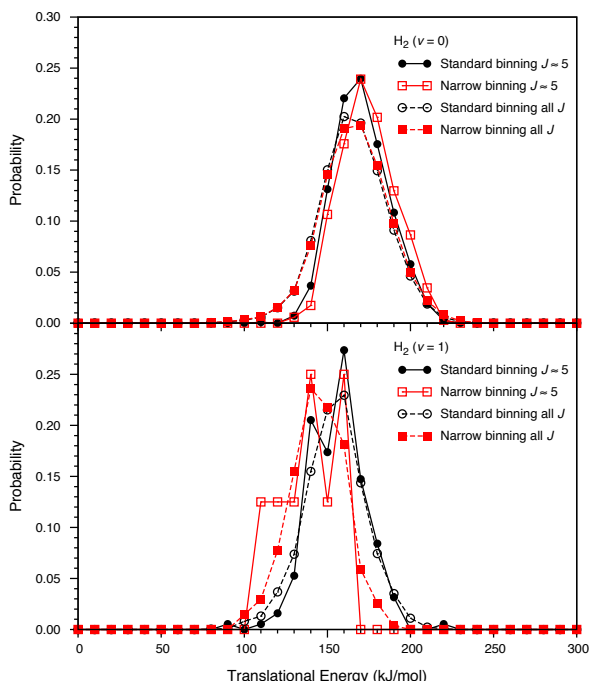

Figure S4. As indicated, QCT $CH_2CO + H_2$ total translational energy distributions, summed over all H_2 J values and for $J \sim 5$, obtained using standard (black lines and black symbols) and narrow (red lines and red symbols) histogram binning of H_2 vibrational states.

Figure S4 shows, for both vibrational states, there is very little angular momentum dependence on the total translational energy distribution; the distributions summed over all J are slightly broader than the $J \sim 5$ distributions. Furthermore, the nature of the binning of H_2 ($v = 0$) does not affect the H_2 ($v = 0$) total translational energy distribution. Similarly to the $J \sim 5$ case, with narrow binning of H_2 ($v = 1$) the translational energy distribution summed over all J, is narrower and centered at lower energy. In all cases, however, no trajectories formed $CH_2CO + H_2$ with less than 55 kJ/mol translational energy.

The constraints given in Table 1 ensured trajectory initial conditions were sampled from an approximation of the transition state dividing surface. Rather than using holonomic constraints based on the eigenvector corresponding to the imaginary frequency at the transition state, simple bond length constraints were used. To test whether these constraints affected the probability distributions a set of 100 000 trajectories were performed constraining only the four bond lengths associated with the four-membered ring at the transition state, all other parameters were as given in Table S1. Of these 34 088 trajectories formed $CH_2CO + H_2$. The resulting H_2 vibrational energy distribution is compared to that obtained using the original five constraints in Figure S2. For standard histogram binning of the H_2 vibrational states, a comparison of H_2 angular momentum distributions and $CH_2CO + H_2$ total translational energy distributions, for the different initial condition constraints, is shown in Figure S5.
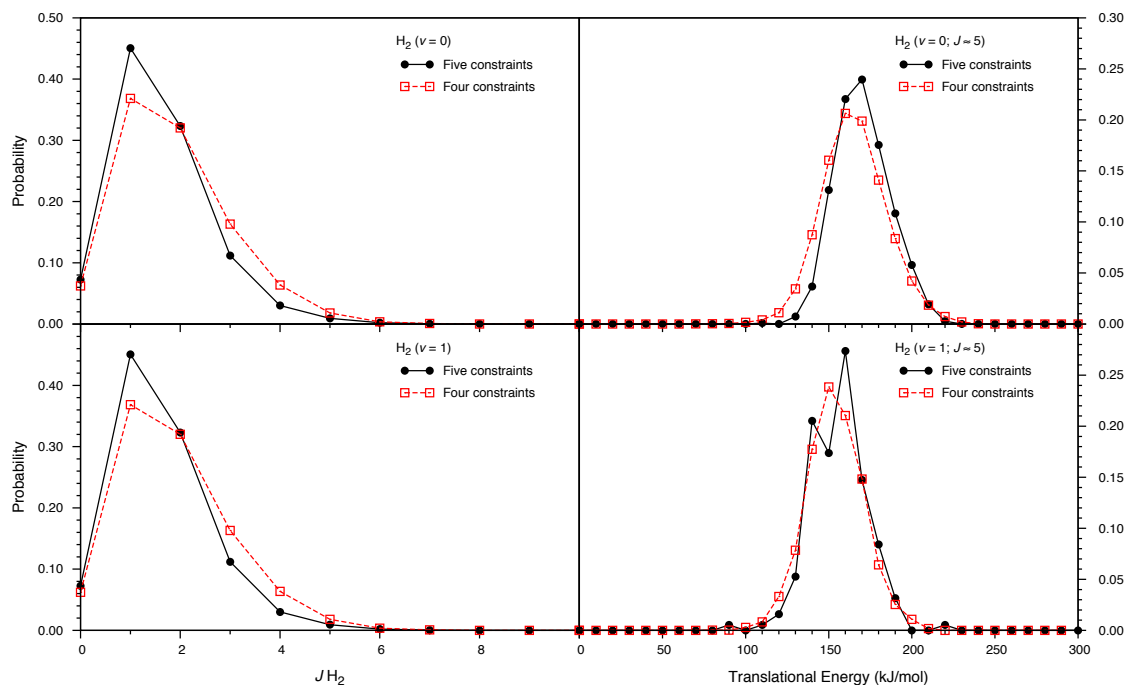

Figure S5. As indicated, QCT H_2 angular momentum (left) and total translational energy (right) distributions obtained using five constrained bond lengths for trajectory initial conditions (solid black lines, solid black circles) and four constrained bond lengths (red dashed lines, open red squares).

Figures S2 and S5 indicate that the nature of the constraints used to define the trajectory initial conditions has little affect on the H_2 vibrational energy distribution or total translational energy distributions. There is a slight increase in H_2 vibrational energy and a slight decrease in $CH_2CO + H_2$ translational energy when fewer constraints are used. The H_2 angular momentum distributions, for both H_2 ($v = 0$, $v = 1$) are slightly hotter and broader with fewer initial condition constraints, they still, however, peak at $J = 1$ and are not consistent with the experimental results shown in Figure 4 of the main text. Similarly, even with more flexible initial conditions, no trajectories form $CH_2CO + H_2$ products with less than 55 kJ/mol translational energy. Thus, neither the nature of the trajectory initial conditions nor the nature of the binning of the H_2 quasiclassical vibrational states have an impact on the interpretation of the experimental results: QCT simulations on a zero-point energy corrected reaction path potential are not consistent with the experimental REMPI and velocity map ion imaging data. This suggests that the $CH_3CHO \rightarrow CH_2CO + H_2$ does not occur via a simple IRC mechanism over the transition state for the reaction.

IV. Pressure dependence of CH_2CO quantum yields

The dependence of CH_2CO quantum yield at 305 nm on neat CH_3CHO pressure was measured in the range 10 to 50 Torr CH_3CHO as shown in Figure S6. The observed quantum yield is independent of pressure with $\phi \approx 0.0075 \pm 0.002$ at all pressures. The error bars mostly reflect the uncertainty in the published ketene IR absorption cross section, which is used to convert experimental absorbance to a number density, and thereby to quantum yield.
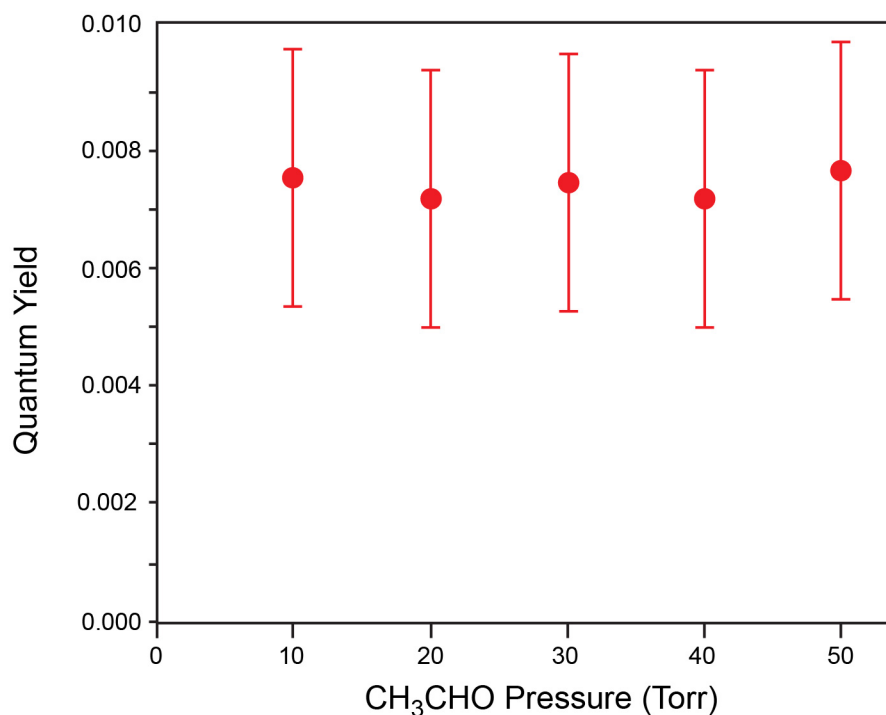
Figure S6: CH_2CO quantum yield as a function of neat CH_3CHO pressure.

V.   References

[1].   D. Townsend, M. P. Minitti, and A. G. Suits, *Rev. Sci. Instrum.* **74** 2530 (2003).

[2].   D. H. Parker, and A. T. J. B. Eppink, *J. Chem. Phys.* **107** 2357 (1997).

[3].   J. Ischtwan, and M. A. Collins, *J. Chem. Phys.* **100** 8080 (1994).

[4].   M. J. T. Jordan, K. C. Thompson, and M. A. Collins, *J. Chem. Phys.* **102** 5647 (1995).

[5].   M. A. Collins, *Theor. Chem. Acc.* **108** 313 (2002).

[6].   K. L. K. Lee, M. S. Quinn, S. J. Kolmann, S. H. Kable, and M. J. T. Jordan, *J. Chem. Phys.* **148**, 194113 (2018).

[7].   L. B. Harding, Y. Georgievskii, and S. J. Klippenstein, J. Phys. Chem. A **114** 765 (2010).

[8].   H. A. Cruse, and T. P. Softley, *J. Chem. Phys.* **122** 124303 (2005).

[9].   B. R. Heazlewood, S. J. Rowling, A. T. Maccarone, M. J. T. Jordan, and S. H. Kable, *J. Chem. Phys.* **130** 054310 (2009).

[10].   T. Kono, M. Takayanagi, and I. Hanazaki, *J. Phys. Chem.* **97** 12793 (1993).

[11].   L. Bonnet and J.-C. Rayez, *Chem. Phys. Lett.* **277**, 183 (1997).

[12].   L. Bonnet and J.-C. Rayez, *Chem. Phys. Lett.* **397**, 106 (2004).

[13].   G. Czakó and J. M. Bowman, *J. Chem. Phys.* **131**, 244302 (2009).

[14].   L. Bonnet, *Int. Rev. Phys. Chem.* **32**, 171 (2013).